Ocean Engineering 285 (2023) 115488

Contents lists available at ScienceDirect

Ocean Engineering

journal homepage: www.elsevier.com/locate/oceaneng

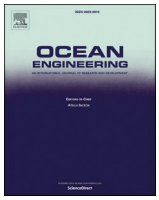

Actuator disk theory and blade element momentum theory for the force-driven turbine

Hongbo Hou [a], Weichao Shi [b,*], Yunxin Xu [a], Yang Song [b]

[a] Department of Naval Architecture, Ocean and Marine Engineering, University of Strathclyde, 100 Montrose Street, Glasgow, G4 0LZ, UK
[b] School of Engineering, Newcastle University, Newcastle Upon Tyne, NE1 7RU, UK

ARTICLE INFO

Keywords:
Force-driven turbine
Actuator disk theory
Blade element momentum theory
Underwater glider

ABSTRACT

The Actuator Disk Theory and the Blade Element Momentum Theory (BEMT) are widely applied in the field of tidal and wind turbine design. The current BEMT turbine design method is based on the assumption of achieving the Betz limit when the axial induction factor (a) reaches $\frac{1}{3}$. But this only applies to turbines driving by a constant velocity, i.e. the velocity-driven turbine. This paper introduces a new type of turbine, namely the force-driven turbine which by its name is driven by a constant force.

This paper then expanded the actuator disk theory for the force-driven turbine and identified the relationship between the axial induction factor with the power and the energy yield of the force-driven turbine. According to the relationship, this paper proposes a new BEMT turbine design method for the preliminary design of the force-driven turbine. Then, a case study is conducted to demonstrate and verify the developed method. The case study shows the newly developed method can be used to quickly and effectively identify the optimum design for force-driven turbines.

1. Introduction

1.1. Velocity-driven turbines

Wind/tidal turbines are devices to convert the kinetic energy in the moving air/water to rotational mechanical energy to be converted to electrical energy by generators. In 1887, Scottish academic James Blyth installed the first wind turbine with electric power generation capability in human history. Since then, modern wind and tidal energy have played an increasingly important role in human life. Two typical types of turbines are widely used nowadays, including the horizontal axis turbine (HAT) and the vertical axis turbine (VAT). Amongst these two types of turbines, the HAT is better practised because it typically has higher power coefficients, simple structure, stable rotation and self-starting ability (Das Karmakar and Chattopadhyay, 2022). In this paper, we mainly focus on the study of HATs.

Currently, for the design of the HAT, most of the HATs are designed by using the Blade Element Momentum Theory (BEMT). BEMT contains two parts, Blade Element Theory and the momentum theory. Blade Element Theory is developed originally for propellers by William Froude (1878) and then expanded to be used for turbines. It breaks the blades down into several segments and then calculates the forces for each segment. These forces are later integrated to obtain the total forces and moments. On the other hand, to understand the changes in the flow field due to the act of these forces and moments, the momentum theory which is also called the actuator disk theory developed by Rankine, W.J.M. (Rankine, 1865), still originally for propellers but later on for turbines. By combining these two fundamental mathematical models, velocity, pressure, forces and moments in each blade segment can be correlated. And the optimal design of the turbine blade can be obtained.

More importantly, in 1919, based upon the actuator disk theory and the principles of conservation of mass and momentum, Betz realised that the turbine's efficiency or power coefficient C_p has a theoretical upper limit which is 59.3%, known as the Betz limit. Furthermore, Betz noticed that for the ideal turbine to achieve the Betz limit, the turbine must be able to reduce the flow velocity by 1/3 (Betz, 1920). The fractional drop in axial flow velocity between the upstream and the turbine rotor is defined as the axial induction factor, a.

Then, the $a = \frac{1}{3}$ becomes the basis of modern turbine design. When designing a turbine based on the BEMT, the first step is to assume that the turbine will be able to reduce the axial flow velocity by $\frac{1}{3}$; and then the turbine's twist angle and chord length can be calculated accordingly

* Corresponding author. School of Engineering, Armstrong Building, Newcastle Upon Tyne, NE1 7RU, UK.
E-mail address: weichao.shi@newcastle.ac.uk (W. Shi).

https://doi.org/10.1016/j.oceaneng.2023.115488
Received 11 May 2023; Received in revised form 20 July 2023; Accepted 29 July 2023
Available online 1 August 2023

to form the design. And this method has been widely practised and well-validated to do the preliminary design of a turbine.

However, this design method is used only for preliminary design nowadays because the actuator disk theory cannot precisely describe the flow around the turbine and ignores many practical problems in engineering. In reality, many factors must be considered in turbine design. For example, these factors include the structure strength of the turbine; a considerable proportion of turbines designed with $a = 0.28$, the value is set less than the optimum ($\frac{1}{3}$) because a substantial load reduction can be achieved with this value, while the reduction in energy yield is fairly slight (Corten and Schaak, 2008). These factors also include the interaction between the turbines in the wind farm; to increase the total energy yield of the wind farm, a promising strategy is to reduce the power production of upwind turbines by changing its a so that downwind turbines can harvest more energy; this method is so called axial induction control (AIC) (Boersma et al., 2017; van der Hoek et al., 2019; Houck and Cowen, 2022). The tip loss is also an important factor influencing the final geometry of the turbine; there are already methods to introduce the tip loss model into the turbine design process to determine the optimal turbine (El Khchine and Sriti, 2017). These advanced design methods developed based on Betz's actuator disk theory can be more suitable for special working conditions, more practical and more accurate, but the fundamental has not changed over time.

Nevertheless, these methods derived from Betz's actuator disk theory are to design a turbine which is driven by a designated incoming velocity which is referred as the velocity-driven turbine. The designed turbine aims to harvest the maximum energy from a moving fluid at a certain speed. Most of the turbines in the wind and tidal energy industry are of this type. The thrust of this type of turbine is only considered in the design of the supporting structure, which doesn't impact energy harvesting. But in this paper, we want to discuss a completely new type of HATs, in which the turbines are driven by a force instead of a velocity.

1.2. Force-driven turbines

Force-driven turbines are a type of turbine which is driven by a force pushing or pulling the turbines to spin. Although the force-driven turbine is uncommon, it has already a long history. The earliest force-driven turbine was invented as a kind of Ram Air Turbine (RAT), which is a turbine installed in aircraft and uses the ram pressure to generate power as a power source (Saad et al., 2017; Jian, 2016). During World War II, Germany developed the first rocket-powered fighter in history which is known as Messerschmitt Me 163 Komet, which is shown in Fig. 1. To solve the power supply problem, it installed an RAT at the nose. As the Messerschmitt Me 163 Komet is propelled forward by a powerful rocket engine, the incoming flow spins the RAT to power the system. This kind of RAT is also used on another rocket-powered fighter Mikoyan-Gurevich I-270 developed by Soviet Air Forces (Gunston, 2000, English).

However, with the advancement of the turbojet engine output, the rocket-powered fighter became unnecessary. Nowadays, the RAT is commonly used as an emergency power source on modern aircraft when both primary and auxiliary power sources are lost (Saad et al., 2021), as shown in Fig. 2.

Another application of the force-driven turbine is a kind of mortar shell that contains a tiny power-generating turbine on its head. It is usually dropped by an unmanned helicopter at a high altitude, which is shown in Fig. 3. When the whole system is driven down by gravity, the turbine is then driven by the airflow and generates power for a proximity fuze.

In the ocean, another application has been observed on the thermal underwater gliders (UGs) to harvest the kinetic energy while the gliders move through the water column. And Jack A. Jones and Yi Chao applied for a patent in 2006 for this concept (Jones and Chao, 2006). Thermal gliders are a type of gliders powered by a thermal buoyancy engine (Wang et al., 2020; Webb et al., 2001; Yang et al., 2016; Ma et al., 2016). The thermal buoyancy engine can convert the thermal energy in seawater to mechanical energy and then use the mechanical energy to generate ballast force to drive the UG to ascend and descend in a sawtooth trajectory in the ocean. The operating principle and the typical working mode of thermal UG are shown in Fig. 4.

The development of thermal UGs is still limited by their limited battery power, which provides energy for their onboard payloads and attitude control systems; the limited volume of the UG hull cannot accommodate large battery packs. The UGs need renewable power. One of the state-of-the-art solutions is to introduce an energy harvesting mechanism which can convert the thermal energy in seawater to electrical energy through hydraulic-based systems (Chao, 2016; Jones et al., 2014; Wang et al., 2019). However, to the authors' knowledge, the patent applied by Jack A. Jones and Yi Chao has not been explored or reported explicitly.

We explored the concept further and proposed a new type of thermal buoyancy engine with high ballast capacity to maximise the energy yield (Shi et al., 2022). The developed energy harvesting mechanism is illustrated in Fig. 5. This new-type thermal buoyancy engine drives the UG moving vertically through the water column and the turbine behind rotates to convert the kinetic energy to electric energy.

Unlike the traditional velocity-driven turbine, this turbine is driven by a ballast force which is determined by the thermal buoyancy engine. So, when designing this turbine, the thrust generated by the turbine shall be considered and the design method for velocity-driven turbines is no longer valid, which motivates the research in this paper.

This paper is organized as follows. Section 2 reviews the traditional

Fig. 1. Messerschmitt Me 163 Komet and its turbine (Bzuk, 2003).

Fig. 2. The Ram Air Turbine (RAT) on modern aircraft (SASHAX41, 2019).

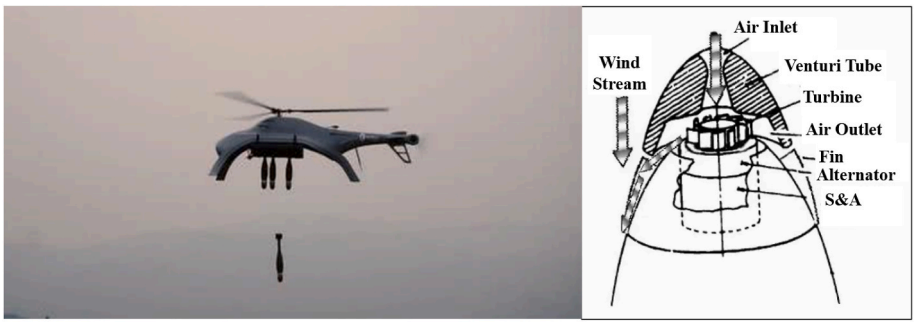

Fig. 3. The mortar shell with energy harvesting turbine (Andersen, 2017; CCTV, 2019).

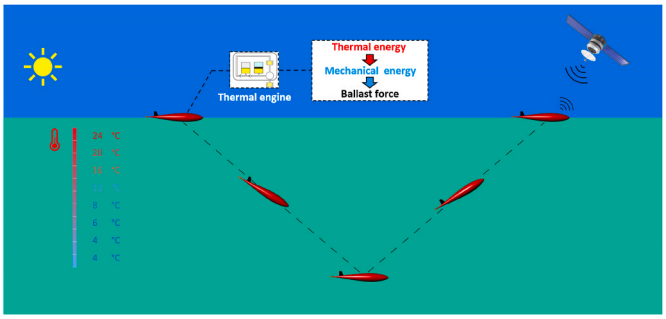

Fig. 4. The working principle and typical working mode of thermal UG.

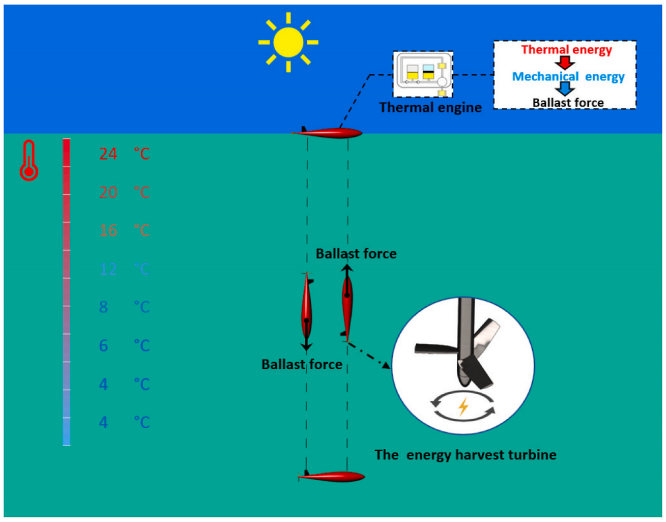

Fig. 5. The working principle of the energy harvesting mechanism.

BEMT design method for the velocity-driven turbine. Section 3 introduced the momentum theory for force-driven turbines and proposes a new BEMT design method. Section 4 is the verification of the developed design method. Finally, section 5 summarises the main conclusions of this work.

2. Betz limit and the traditional BEMT design method

2.1. Actuator disk theory and betz limit

Based on the momentum theory, Betz's work pioneered the use of the actuator disc model and defined the theoretical limit of velocity-driven turbines in open flow (Betz, 1920). In this model, the turbine is simplified as an actuator disc in one dimension, this actuator disc creates a discontinuity in the pressure of the fluid flowing through it and harvests energy from the flow (Zhao et al., 2019; Dixon and Hall, 2010), and only the exchange of momentum between the flow and the disc in the axial direction of the disc is analysed (De Lellis et al., 2018), the model is shown in Fig. 6.

The model has several assumptions: (a) the flow is irrotational, steady, incompressible, homogenous, and inviscid. (b)the thrust on the actuator disc is uniform. (c) The wake is not rotational. (d) The blade number is unlimited. (e)the static pressures far upstream and far downstream of the disc are equal to the undisturbed environment static pressure (De Lellis et al., 2018; Zhao et al., 2019).

In the model shown in Fig. 6, the U is the flow velocity, the P is the pressure, P^+ is the pressure in front of the disc and the P^- is the pressure behind the disc. The symbol ∞ at subscript indicates the condition far upstream, the d at subscript indicates the condition at the disc, and the W at subscript indicates the condition far downstream.

With U_∞ and U_d, the axial induction factor, a, can be expressed by Eq. (1):

$$a = \frac{U_\infty - U_d}{U_\infty} \tag{1}$$

The relationship between a and the power coefficient (C_p) and the thrust coefficient(C_T)of the turbine can be derived using the momentum theory (Betz, 1920):

As shown in Fig. 6, the streamtube keeps expanding from upstream to downstream. In the streamtube, according to the mass conservation law, the mass flow rate keeps the same everywhere, therefore

$$\rho A_\infty U_\infty = \rho A_d U_d = \rho A_W U_W \tag{2}$$

where ρ is the flow density, A_∞ is the cross-section of the stream-tube at far upstream, A_d is the cross-section of the streamtube at the disc, A_W is the cross-section of the streamtube at far downstream.

As mentioned above, the flow passing through the actuator disc is being slowed down, which leads to the momentum change rate of the flow expressed by the:

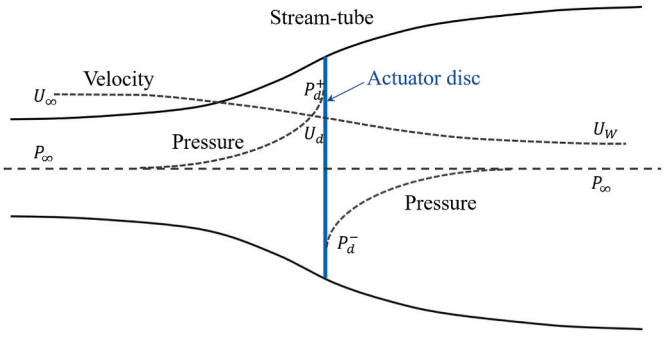

Fig. 6. Side view of actuator disc and streamtube model.

$$Momentum\ change\ rate = (U_\infty - U_W)\rho A_d U_d \tag{3}$$

The force that leads to this momentum change rate is due to the pressure difference before and after the actuator disc. Therefore

$$(P_d^+ - P_d^-)A_d = (U_\infty - U_W)\rho A_d U_\infty (1-a) \tag{4}$$

Then, apply Bernoulli's equation to the flow in the streamtube. Bernoulli's equation is based upon the principle of energy conservation, which explains that the total energy of the fluid along the flow of the stream is equal to all points of the steady flow; this means that the total energy of the kinetic, potential and internal energies in the streamline is constant (Batchelor, 2000). Bernoulli's equation can be expressed by:

$$\frac{1}{2}\rho U^2 + P + \rho g h = Constant \tag{5}$$

Considering the total energy is different upstream and downstream, Bernoulli's equation is applied to the upstream and downstream of the stream-tube individually.

Applying Bernoulli's equation in the flow upstream leads to

$$\frac{1}{2}\rho U_d^2 + P_d^+ = \frac{1}{2}\rho U_\infty^2 + P_\infty \tag{6}$$

Applying Bernoulli's equation in the flow downstream leads to

$$\frac{1}{2}\rho U_d^2 + P_d^- = \frac{1}{2}\rho U_w^2 + P_\infty \tag{7}$$

By equating Eq. (6) and Eq. (7), we can write

$$(P_d^+ - P_d^-) = \frac{1}{2}\rho(U_\infty^2 - U_W^2) \tag{8}$$

By equating Eq. (4) and Eq. (8), we can write

$$\frac{1}{2}\rho(U_\infty^2 - U_W^2)A_d = (U_\infty - U_W)\rho A_d U_\infty (1-a) \tag{9}$$

From Eq. (9), we can get

$$U_W = (1-2a)U_\infty \tag{10}$$

Eq. (10) indicates that 50% of the flow velocity reduction occurs upstream, and another 50% occurs downstream (Burton et al., 2011, Tony Burton et al., 2011).

By equating Eq. (4) and Eq. (10), we can get the thrust (T) acting on the actuator disc by Eq. 11

$$T = (P_d^+ - P_d^-)A_d = 2\rho A_d U_\infty^2 a(1-a) \tag{11}$$

The thrust coefficient (C_T) can be expressed by Eq. 12

$$C_T = \frac{T}{\frac{1}{2}\rho U_\infty^2 A_d} \tag{12}$$

With Eq. (12), we can get the relationship between the C_T and the a which is expressed by Eq. 13

$$C_T = 4a(1-a) \tag{13}$$

The power (P) is the work done by the T per second; therefore, the P equals TU_D and can be expressed by Eq. 14

$$P = TU_D = 2\rho A_d U_\infty^3 a(1-a)^2 \tag{14}$$

The power coefficient (C_P) can be expressed by Eq. 15

$$C_P = \frac{P}{\frac{1}{2}\rho U_\infty^3 A_d} \tag{15}$$

So, we can get the relationship between the C_P and the a which is expressed by Eq. 16

$$C_P = 4a(1-a)^2 \tag{16}$$

The relationship between C_T , C_P and a is shown in Fig. 7. The maximum value of C_P is about 0.5926, known as the Betz limit. It is the theoretical maximum efficiency for any turbine (Burton et al., 2011).

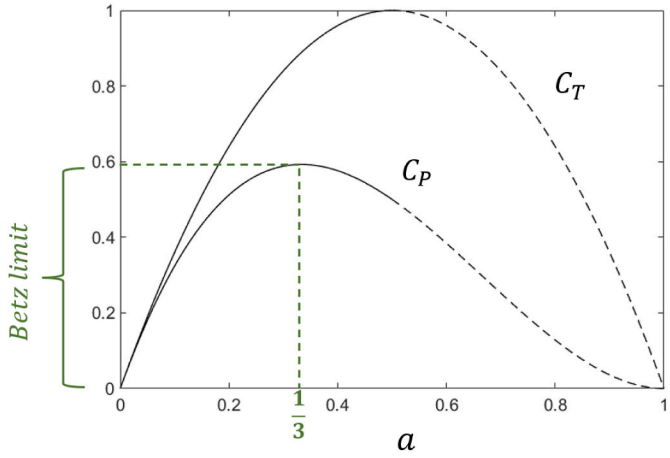

Fig. 7. The relationship between C_P, C_T and a.

Also shown in Fig. 7, the a corresponding to the Betz limit is $\frac{1}{3}$. This value can be obtained by computing the root of the function $\frac{dC_P(a)}{da}$ (De Lellis et al., 2018). It means for an ideal turbine to achieve the highest C_P, the turbine must reduce the flow velocity in front of it by $\frac{1}{3}$ of U_∞. This conclusion is the base of the BEMT design method.

2.2. Blade element momentum theory

Betz simplified the turbine as an actuator disc to determine the optimal a for the turbine to achieve the highest C_p based upon the momentum theory (Betz, 1920). However, the real turbine is a structure with a number of blades. To determine the optimal geometry of the blades, the momentum theory needs to be combined with the blade element theory. In blade element theory, the turbine blade is divided into several individual segments, this theory assumes that the forces acting on the blade segment can be calculated by the two-dimensional lift coefficient (C_L) and drag coefficient (C_D) of the blade element using the angle of attack (AoA) determined by the incident resultant flow velocity on the blade element. The three-dimensional effects and the velocity component of flow in the spanwise direction of the blades are ignored (Burton et al., 2011).

The velocity triangle on a blade element in the frame of reference of the turbine shown in Fig. 8(a) indicates the relationship between the blade element and the flow acting on it. The $\varnothing$ is the inflow angle, α is the angle of attack, β is the twist angle, a' is the tangential induction factor indicating the fractional increase in tangential flow velocity, W is the relative velocity. λ is the tip speed ratio, which is the ratio of the turbine tip rotational velocity to U_∞, R is the radius of the turbine, r_e is the distance between the blade element and the axis of rotation.

The force on the blade element is shown in Fig. 8(b), the L and D are the lift and drag respectively, which are determined by the blade element's hydrodynamic characteristic coefficients C_L and C_D vary with the angle of attack (AoA). After calculating the force on each blade element, the thrust and torque of the turbine can be obtained by integrating the forces on these elements.

2.3. The traditional BEMT design method

Following the development of BEMT, the ideal turbine and its design method can be obtained based on the fore-mentioned Betz limit. This method first sets the value of the axial induction factor, a, to be $\frac{1}{3}$ expecting the designed turbine can achieve the theoretical upper limit in efficiency. Here we use a_{design} to describe the design axial induction

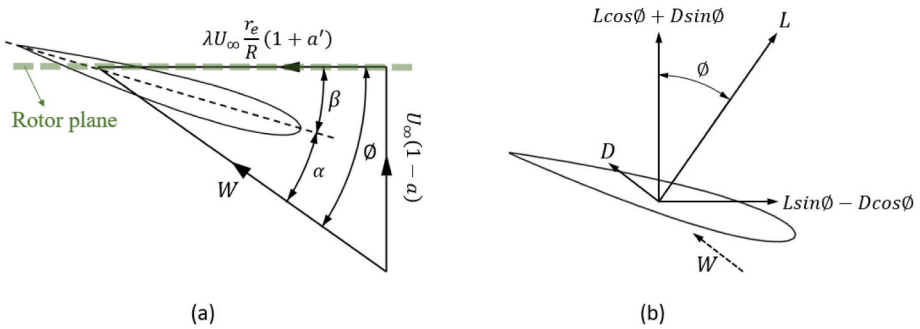

Fig. 8. a) Velocities relating to the turbine blade, b) Force on blade element.

factor, as shown in Eq. (17).

$$a_{design} = \frac{1}{3} \tag{17}$$

Then, according to the angular momentum theory (Burton et al., 2011), we can derive the relationship between the a and a' and calculate the design tangential induction factor (a'_{design}). The tangential induction factor corresponding to the a_{design} is defined as a'_{design} and expressed by Eq. (18).

$$a'_{design} = \frac{a_{design}(\mathbf{1} - a_{design})}{\lambda_{design}{}^2 \mu^2} \tag{18}$$

where the λ_{design} is the design tip speed ratio. μ is the ratio of the local radius r_e to the total radius R, $\frac{r_e}{R}$.

Then calculate the design inflow angle ($\varnothing_{design}$) with Eq. (19), such that:

$$\varnothing_{design} = \arctan\left(\frac{1 - a_{design}}{\lambda_{design}\mu\left(1 + a'_{design}\right)}\right) \tag{19}$$

Then, the optimal twist angle (β) can be calculated by Eq. 20

$$\beta = \varphi - \alpha_{design} \tag{20}$$

where the α_{design} is the design angle of attack.

Under the governing of the BEMT, the angular momentum change in a unit of time at each sectional radius calculated is equal to the torque generated by the corresponding segment. This relationship yields Eq. (21) for calculating the chord length (C), such that:

$$C = \frac{8\pi\lambda_{design}\mu^2 a'_{design}(1 - a_{design})RU_\infty^2}{N(C_L \sin\varnothing - C_D \cos\varnothing)W^2} \tag{21}$$

where N is the blade number.

Since the design premise of the value of C and β is $a_{design} = \frac{1}{3}$, when the turbine is under design working condition, the a of the turbine with the designed C and β will be or close to $\frac{1}{3}$, which will lead to the highest C_P according to Betz's theory. As mentioned above, this design method is widely practised and well-validated to do the preliminary design of a turbine nowadays.

3. Optimal a and design method for force-driven turbine

For the force-driven turbine in the energy harvesting mechanism shown in Fig. 5, the relationship between C_p and a is still under the govern of Betz's theory; the maximum C_p of the force turbine is still 59.3%, and the a corresponding to maximum C_p is still 1/3; however, the velocity (U) passing through and driving the force-driven turbine is the velocity of the platform, which is also a function of the thrust generated by the turbine linking with the axial induction factor, a. For example, the higher the a is, the more momentum the turbine extracts from the flow, which leads to higher thrust dragging the velocity down. As a result, the highest C_p of the force-driven turbine does not necessarily lead to the highest power (P) nor the highest energy yield (E_y). This means that $a = \frac{1}{3}$ is no longer a prerequisite for the force-driven turbine and how to design the turbine for this purpose is unknown.

In the following part, we try to re-establish the actuator disk theory and the BEMT theory for the force-driven turbine finding the relationships between the power P, the energy E_y and the axial induction factor a. We expand and propose a new BEMT design method, aiming to determine the optimal geometry of force-driven turbines.

3.1. Expansion of the actuator disk theory for the force-driven turbine

3.1.1. The optimal a for power

As shown in Fig. 9, the carrying platform of the force-driven turbine is currently identified as mostly the axisymmetric body, i.e. the underwater glider. Here the radius of the turbine is defined as R. The thrust coefficient of the turbine is C_T. The radius of the carrying platform is defined as r. The resistance coefficient of the platform body is defined as C_d.

To study the relationship between the a, P and E_y of the force-driven turbine, the turbine in the energy harvesting mechanism is also simplified as an actuator disc in the same way as Betz's theory(Betz, 1920) introduced above. When the system is harvesting energy by driving the turbine up and down in the ocean, the system's ballast force (B) equals the sum of the turbine thrust and platform resistance, as shown in Fig. 9. It can be expressed as Eq. (22):

$$B = C_T \frac{1}{2}\rho U^2 \pi R^2 + C_d \frac{1}{2}\rho U^2 \pi r^2 \tag{22}$$

where ρ is the fluid density, U is the moving velocity of the whole platform.

According to the actuator disc theory, we can establish the function between the a and the C_T as shown in Eq. (13). Substituting Eq. (13) into Eq. (22) we can derive the moving velocity (U) in below Eq. (23). We can see now the flow velocity through the turbine will be varying with different designs of turbines and platforms, which will directly impact on the energy can be harvested.

$$U = \sqrt{\frac{B}{\frac{1}{2}\rho\pi R^2\left(4a(1-a) + C_d\frac{r^2}{R^2}\right)}} \tag{23}$$

To calculate the maximum power that the system can harvest, by substituting Eq. (23) into Eq. (14) we can see the power P of the force-driven turbine is a function of a as shown in Eq. (24).

$$P(a) = B^{\frac{3}{2}}\left(\frac{1}{2}\rho\pi R^2\right)^{-\frac{1}{2}} \frac{4a(1-a)^2}{\left[4a(1-a) + C_d\frac{r^2}{R^2}\right]^{\frac{3}{2}}} \tag{24}$$

It can be seen that P is a function of B, R, r, C_d, and a. For a specific

a. Ascending (Gravity<Buoyancy) b. Descending (Gravity>Buoyancy)

Fig. 9. Forces of the underwater glider during the energy harvesting.

carrying platform, the ballast force B and the platform radius r will be defined at the beginning according to the mission requirement which includes the payload, the volume of the inner units, etc; therefore, we set these as 1 to have a non-dimensional power. So we can see the power is only relating to R, C_d and a. To study the relationship between the P, R, C_d and a, we calculated the P of different combinations of R, C_d and a within a reasonable range in the real world to show their relationship; the result is shown in Fig. 10 where the C_d is from 0 to 0.4, a is from 0.01 to 0.5, the R is from 0.1 to 2, the space is coloured by power.

From Fig. 10, we can observe that the P decreases with the increase of the C_d; and the P doesn't change monotonically with the change of R. Most significantly, from the section of $R = 1$, it can be observed that the P is depending on the axial induction factor (a). To further understand this change, Fig. 11 presents the corresponding conditions for the peak power to be achieved, it can be observed that the optimal a for the peak power decrease with the increase of R and increase with the increase of C_d.

Based on the derivations in the last section, a question arises regarding the maximum energy yield. Whether the maximum energy yield can be achieved in the maximum power. Considering the use case of the thermal glider, gliders harvest thermal energy and perform dives to drive the turbine. Here, this paper considers the energy yield in the

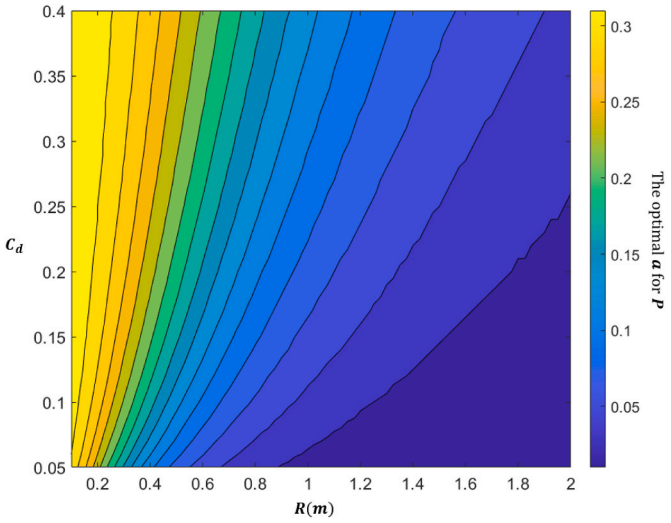

Fig. 11. The optimum a with the highest P at different C_d and R 3.1.2 The optimal a for Energy.

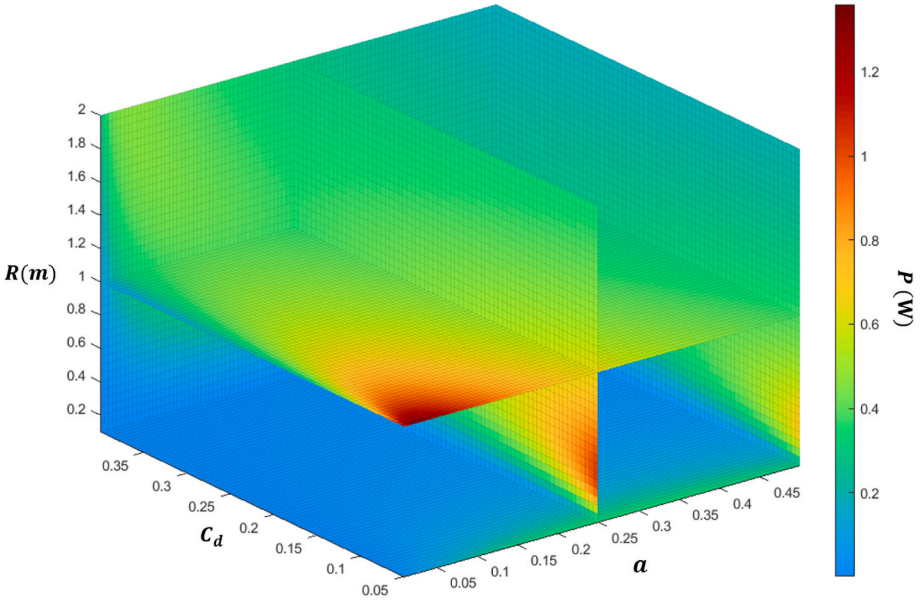

Fig. 10. The relationship between the R, C_d , a and P.

individual operation cycle and discusses the relationship between the energy yield and the a.

The operation cycle time(t)of the force-driven turbine in one dive & ascend cycle can be expressed by Eq. (25):

$$t = \frac{L}{U} \tag{25}$$

where L is the working distance which is twice the working depth of the thermal gliders.

Then, the E_y can be expressed by:

$$E_y = P\frac{L}{U} \tag{26}$$

Equating Eq. (23), Eq. (24) and Eq. (26), results:

$$E_y(a) = BL\frac{4a(1-a)^2}{4a(1-a) + C_d\frac{r^2}{R^2}} \tag{27}$$

We define the work input by the carrying platform as W. According to the definition of work, the W can be expressed by Eq. 28

$$W = BL \tag{28}$$

Equating Eq. (27) and Eq. (28), the relationship between E_y and W can be defined as:

$$E_y = W\frac{4a(1-a)^2}{4a(1-a) + C_d\frac{r^2}{R^2}} \tag{29}$$

It can be seen that E_y is a function of L, B, R, r, C_d, and a. As mentioned in the last section, for a specific carrying platform, ballast force B, the platform radius r and working length L will be defined according to the mission requirement; here, we set these as 1 to have a non-dimensional E_y. Therefore, we can see the E_y is only relating to R, C_d and a. To study the relationship between the E_y, R, C_d and a, Fig. 12 plots the E_y regarding to R, C_d and a.

From Fig. 12 and Eq. (29), it is important to notice that the E_y increases with the increase of R which is clearly opposite to the trend of the P as observed in Fig. 10. Therefore, a balanced design is needed when choosing the radius for the turbine. The turbine with a larger diameter can harvest more energy in a cycle but slowly. However, practically the larger diameter will risk accidental collision and hence damage to the blades; furthermore, the power of the turbine might also be too low to be harvested by any generators. This is a major difference from the velocity-driven turbine and a critical consideration in the design process.

On the other hand, similar to the P, we can observe that the E_y decreases with the increase of the C_d and the highest E_y will no longer peak at a = 1/3. Fig. 13 explains the corresponding conditions for the peak E_y to be achieved. The optimal a for the peak E_y, like for the peak P, decreases with the increase of R and increases with the increase of C_d.In traditional actuator disk theory for the velocity-driven turbine, the C_p describes the efficiency. Higher C_p leads to higher E_y. However, as mentioned above, for the force-driven turbine, the highest C_p may not necessarily lead to the highest energy yield E_y. So, a new parameter for the energy harvest efficiency is needed for the force-driven turbine. In this paper, we define η_m as the efficiency for force-driven turbines, which is presented in Eq. (30).

$$\eta_m = \frac{E_y}{W} = \frac{4a(1-a)^2}{4a(1-a) + C_d\frac{r^2}{R^2}} \tag{30}$$

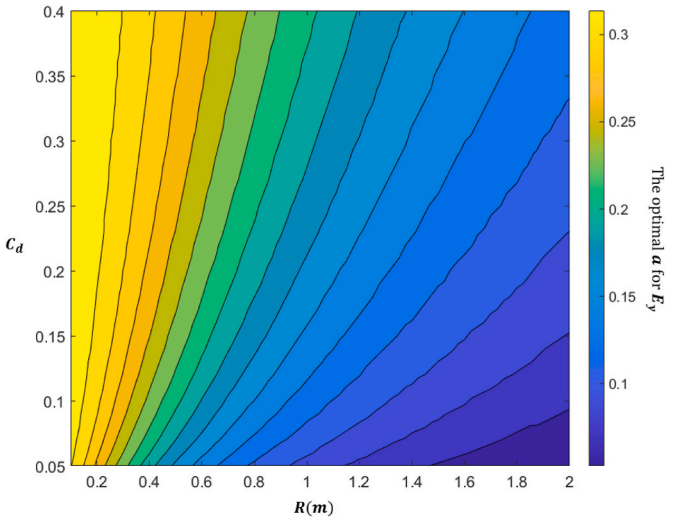

Fig. 13. The corresponding a for the highest E_y at different C_d and R 3.1.3 The efficiency η_m.

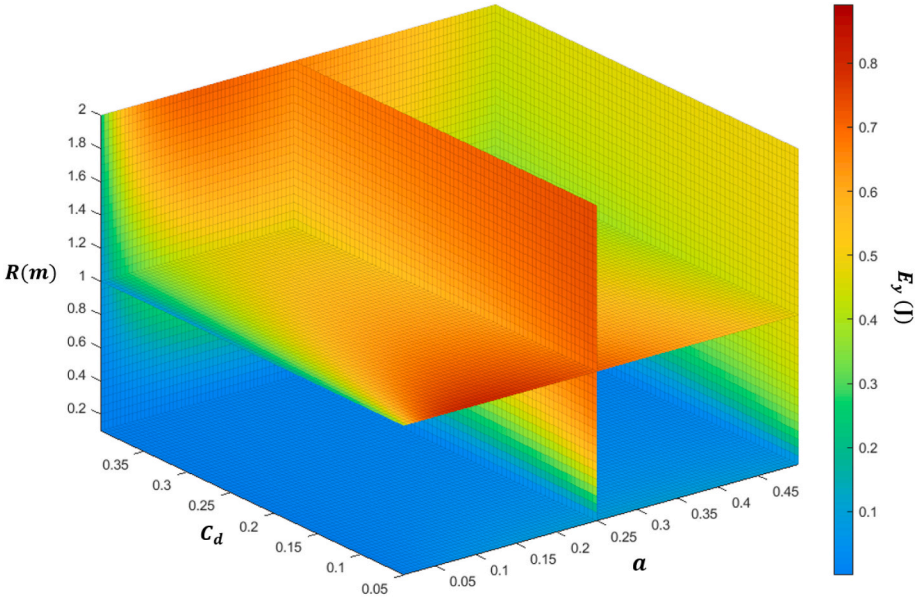

Fig. 12. The relationship between the R, C_d, a and E_y.

It can be seen that the optimal a derived from the Betz limit no longer applies to the force-driven turbine, because the optimal a turns to the root of $\frac{d\eta_m(a)}{da}$ from the root of $\frac{dC_P(a)}{da}$. The maximum efficiency that a force-driven turbine can reach is depending on the resistance coefficient of the carrying platform, the radius ratio between the carrying platform and the turbine and the turbine's axial induction factor. And the efficiency no longer peaks at $a = 1/3$.

3.2. Development of the BEMT-based design method for the preliminary design of the force-driven turbine

The preliminary design method of the force-driven turbine will be varied from the preliminary design method for the velocity-driven turbine shown in section 2.2. The new design flowchart is shown in Fig. 14: Step 1 is to determine the three design parameters of the carrying platform and the turbine, including the C_d , r and R; Step 2, decide the design goal; Step 3, determine the a_{design} by calculating the root of the function $\frac{dP(a)}{da}$ or $\frac{d\eta_m(a)}{da}$, which are named as a_{design_P} and a_{design_E} to distinguish respectively; Then, calculate the optimal C and β with the a_{design} using the BEMT design method introduced in section 2.2.

It is worth pointing out that this design method has great significance only when the projected area of the turbine and the hull in the direction of incoming flow is of the same magnitude. If the hull's projected area or radius is much larger than the turbine, the turbine cannot have a significant impact on the moving velocity of the system, the operating state of this turbine will be closer to a velocity-driven turbine. And the turbine will work more like the actuator disc in Betz's theory, whether it pursues the highest P or E_y, its optimal a will be close to 1/3. This phenomenon can be observed in Figs. 11 and 13, the optimal a will be close to 1/3 with the decrease of turbine radius. Therefore, for the RAT in the rocket-powered fighter shown in Fig. 1, which is much smaller than the hull size, this design method can only slightly change the optimal a in Betz's theory and bring a negligible increase of P or E_y.

4. Verification

In the above, we derived the relationship between the a, P, E_y for the force-driven turbine. The relationship shows the conclusion that the $a = \frac{1}{3}$ no longer leads to the highest P and E_y for a force-driven turbine, which is different from Betz's theory for the velocity-driven turbine. And the optimum power and energy require different turbine designs. Then we proposed a new BEMT design method for the force-driven turbine with separate goals towards maximum power or maximum energy. The next step is to verify the new design method with a case study.

Section 4 is organized in this as follows: In section 4.1, the principle of the BEMT analysis code is introduced with the case study configuration and the procedure of the verification; In section 4.2, the results are presented and discussed.

4.1. The verification method

4.1.1. The BEMT analysis method

In the verification, we use the BEMT analysis method to analyse the energy conversion performance for the designed turbines. Firstly, a and a' are set to zero as the initial condition. Then the inflow angle (φ) is calculated by Eq. (19), but the λ_{design} will be replaced by the operating tip speed ratio ($\lambda_{operating}$). Afterwards, the angle of attack (α) can be calculated with Eq. (20), which can be used to determine the C_L and C_D for every foil segment. Then, the tangential coefficient (C_t) and the normal coefficient (C_n) of each foil segment can be calculated with Eqs.(31) ~32)

$$C_n = C_L \cos\varnothing + C_D \sin\varnothing \tag{31}$$

and

$$C_t = C_L \sin\varnothing - C_D \cos\varnothing \tag{32}$$

Then, calculate the chord solidity (σ_r) by Eq. 33

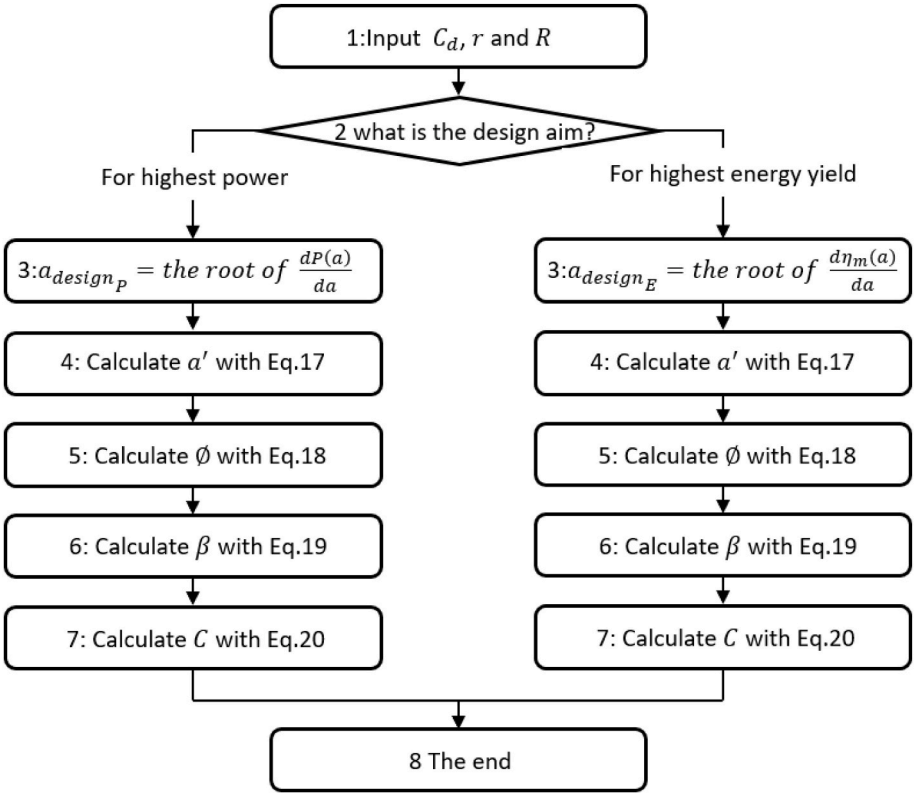

Fig. 14. the flowchart of the new BEMT design method for the force-driven turbine.

$$\sigma_r = \frac{NC}{2\pi\mu R} \tag{33}$$

With C_n and C_t, the a and a' of the flow acting on the foil segment can be calculated by Eqs. (34) and (35).

$$a = \frac{1}{\frac{4\ sin^2\ \varphi}{\sigma_r C_n} + 1} \tag{34}$$

$$a' = \frac{(1-a)\sigma_r C_t}{4\lambda_{operating}\mu\ sin^2\ \varphi} \tag{35}$$

Then, the newly calculated a and a' are used to replace the previous a and a' and the calculation procedure restarts. The iteration stops until the residual of a and a' is less than 0.01 in this case study.

Once the iteration is completed, the result from the iteration, including W, C_t and C_n will be used to evaluate the torque (δQ) and the thrust (δT_b) for each blade element using Eqs. (36)~37)

$$\delta Q = \frac{1}{2}\rho W^2 NCC_t r\delta r \tag{36}$$

$$\delta T_b = \frac{1}{2}\rho W^2 NCC_n \delta r \tag{37}$$

Then, the overall thrust (T_b) and power (P) of the turbine can be obtained by integration. Finally, the C_T and C_P can be calculated by Eq. (12) and Eq. (15), respectively.

To make the BEMT analysis code more accurate, two widely used engineering corrections for the load on blades have been incorporated into the BEMT analysis code in this work. The corrections include Prandtl's tip loss correction (Glauert, 1935; Shen et al., 2005), turbulent wake state correction (Buhl, 2005).

4.1.2. Reference carrying platform of the verification study

Three parameters of the energy harvest mechanism, including C_d, r and R, are determined by the carrying platform. In this case, a typical UG with a classic hull is selected as the platform; the hull shape is shown in Fig. 15. The radius of the platform (r) is 0.1 m. The CFD simulations are conducted to determine C_d of the hull by using the software STAR-CCM+. In the simulation, the unsteady incompressible Reynolds-Averaged Navier Stokes (URANS) model and the K-ω Shear Stress Transport (K-ω SST) turbulence model are selected. A rectangular computational domain is chosen to analyse the flow around the UG hull, the domain and the boundary conditions are shown in the appendix of Fig. 24. The selected domain dimensions adhere to ITTC recommendations (ITTC, 2011). Polyhedral mesh is employed to constitute the simulation domain. The result shows that the C_d is around 0.2 in a wide speed range from 1 m/s to 4 m/s; for simplicity, the C_d of is set as 0.2. And the ballast force (B) is set as 25 N. After the consideration of the balance between the E_y, P and risk of accidental collision, the turbine radius (R) is set as 0.15 m. The blade number (N) is set as 3.

To simplify the analysis, there are two assumptions. First, the hydrodynamic impact of the wake behind the platform can be ignored. The turbine is installed behind the carrying platform, which will be affected by the wake flow of the platform. However, this effect is negligible as the carrying platforms are generally streamlined symmetrical bodies with a low wake shadowing effect.

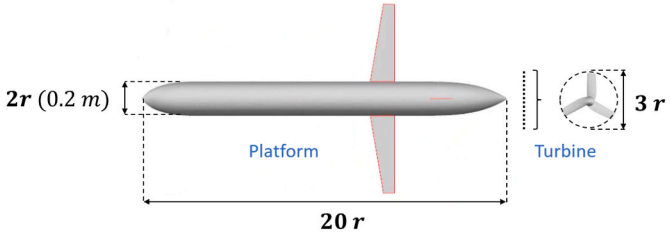

Fig. 15. The carrying platform and the turbine for the case study.

Second, the influence of a varying Reynolds number (Re) on the turbine section is ignored. The Re of the blades may change with different designs and operation conditions. However, this is minimum within a certain range of variation. Therefore, it is neglected in this specific case. The C_L and C_D characteristics of the blade sections have been kept the same over different Reynolds numbers. The foil section of the turbine blades is NACA0015 with C_L and C_D shown in Fig. 16, where the C_L and C_D of the foil are from the simulation of the software XFoil. The design angle of attack (α) is set as 6°, where the foil has the highest lift-to-drag ratio. λ_{design} is set as 4, which is a normal λ_{design} for tidal turbine (Encarnacion et al., 2019).

4.1.3. The procedure of the verification

In this verification, the turbine has been firstly designed using all the possible axial induction factors and then the designed turbines have been analysed with the carrying platform at all the possible operational conditions. In this way, the developed design method can be compared and verified with the optimum solutions to gain confidence for the developed method. The procedure of the verification is shown in Fig. 17, which can be divided into 12 steps.

Step 1Input the design parameters of the carrying platform and the turbine, including: C_d, r, R, C_L, C_D, λ_{design} , N and B.
Step 2& Step 10: Step 2 and Step 10 form a loop; this loop can input a set of a to design and build all the possible turbine blades to be analysed in all the possible working conditions. Here in this study the investigated range of a is from 0.01 to 0.5 with an interval of 0.001, so 491 different a in total and hence 491 different turbines have been simulated to find the optimum design.
Step 3Set the a as a_{design}.
Step 4Generate a turbine with a_{design} based upon the BEMT design method shown in section 2.2.
Step 5and Step 9 form a loop simulating different working conditions for the turbine generated from Step 5: The working conditions mean the different operating tip speed ratios ($\lambda_{operating}$). The range of $\lambda_{operating}$ is from 1 to 7 with an interval of 0.25.
Step 6 to Step 8 is for analysing the η_m of the turbine under a specific λ_o. The detail of these three steps is introduced below.
Step 6Analyse the C_P and C_T based upon the BEMT analysis method introduced in section 4.1.1.
Step 7Compute the moving velocity of the system velocity (U), the power (P), the work time (t) and the energy conversion efficiency (η_m) of the turbine.
Step 9Output the highest η_m and P of a turbine among all the possible λ_o.
Step 11Compare the result with the result obtained using the new method.

4.2. The result of the verification

In Fig. 18, two curves are presented. First, it is the theoretical value of the η_m from Eq. (30) based on the actuator disk theory, demonstrating the relation of η_m and a. Second is the analysed maximum value of the η_m using the above BEMT method at all possible a. Similarly, in Fig. 19, the theoretical value of the P from Eq. (24) based on the actuator disk theory and the analysed maximum P with all the possible a are shown.

The results in Figs. 18 and 19 clearly show that $a = \frac{1}{3}$ no longer leads to the highest energy yield nor the highest power for the force-driven turbine. This confirms our previous findings based on the actuator disc theory. In this specific case study, the analysis result shows that the $a_{design} = 0.101$ leads to the highest η_m and $a_{design} = 0.038$ results in the highest power.

From the result of these 491 turbines in Figs. 18 and 19, we can

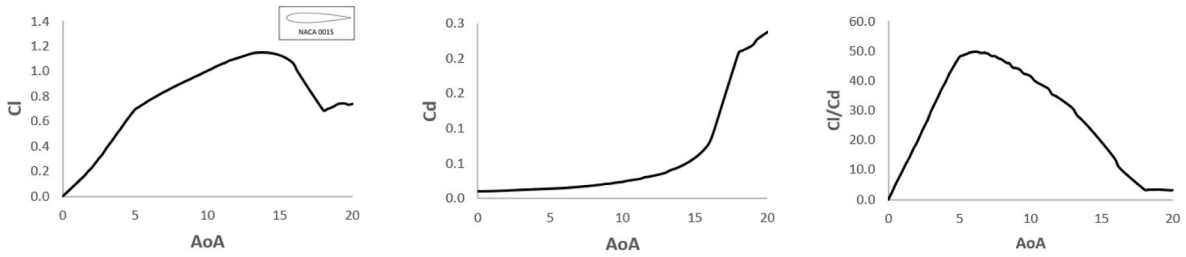

Fig. 16. The lift coefficient, the drag coefficient and the lift-drag ratio of NACA 0015.

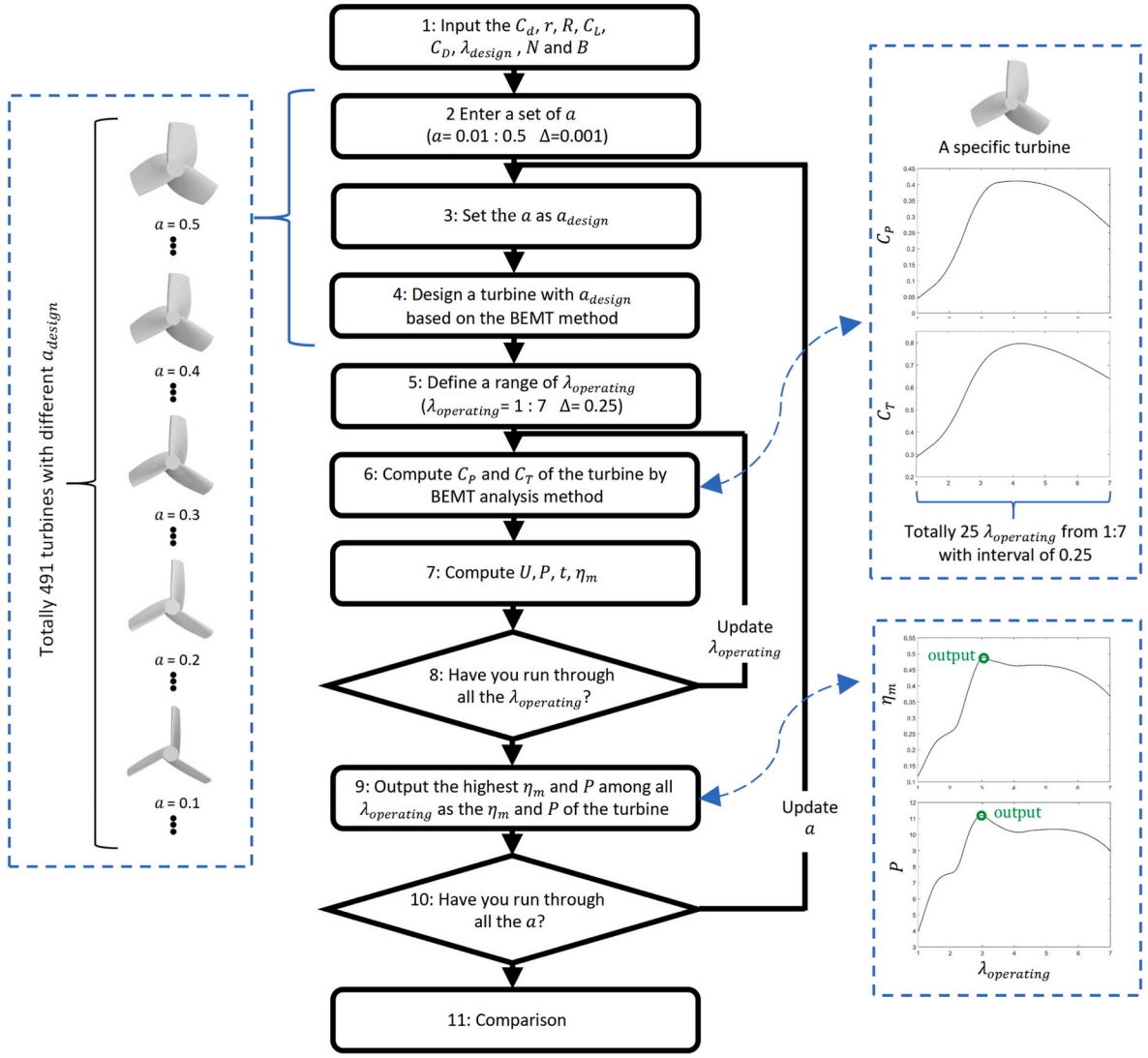

Fig. 17. The flowchart of the verification study finding the optimum turbine in the operational conditions.

observe that the η_m and the P based on the actuator disc theory are always higher than the η_m and the P from the analysis. It is because the actuator disc theory is based upon several ideal assumptions, such as a non-rotating wake, an unlimited number of blades, steady and inviscid flow, Etc. As a result, for the force-driven turbine, η_m and the P based on actuator disc theory can be accepted as the theoretical upper limits for force-driven turbines. These two upper bounds are determined by the C_d of the platform and the radius ratio. These two upper bounds are easy to be estimated in the design stage and have clear indications to guide the design metrics of the energy harvesting mechanism at the early design stage. As an example, in Fig. 18, we can see the upper boundary of η_m is 0.727, while the highest η_m among all the 491 turbines is 0.628. On the other hand, as shown in Fig. 19, the upper limit of P in this case study is 25.66 W, while the highest P among all the turbines is 23.35 W.

From Figs. 18 and 19, we can see that the variation trends of η_m and the P from actuator disc theory and η_m and the P from the analysis are very close. Correspondingly, as shown in Fig. 18, if aiming for the highest E_y, the a_{design_E} is 0.126 based on the actuator disk theory, while the BEMT analysis method shows it can be achieved at a_{design} = 0.101. But the difference caused by the shift of a_{design} is minimum. Therefore the a_{design_E} based on the actuator disk theory is feasible and effective to be used to design the turbine for the highest energy yield. As shown in

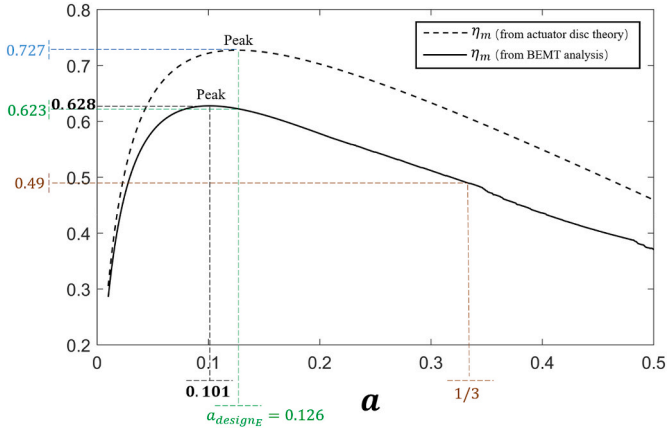

Fig. 18. The η_m based on actuator disc theory and the η_m from the analysis.

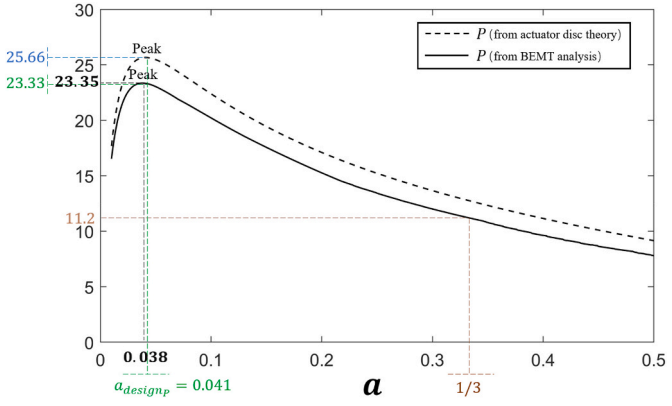

Fig. 19. The P based on actuator disc theory and the P from the analysis.

Fig. 19, aiming for the highest P, the a_{design_P} is 0.041 based on the actuator disk theory, and the BEMT analysis method shows it can be achieved at $a_{deign} = 0.038$ which is very close to the predicted value.

Furthermore, Fig. 20 and Fig. 21 compare the dimensionless chord length ($\frac{C}{R}$) and the twist angle (β) along the radius between the optimal-energy-turbine found amongst all the possible designs, the turbine designed with the optimal a for energy based on the expanded actuator disk theory and the turbine designed with $a = 1/3$. It can be seen that the designed turbine with the expanded actuator disk theory for the force-driven turbine is very close to the optimal design; therefore, the developed theory has been verified to be effective in finding the optimal design.

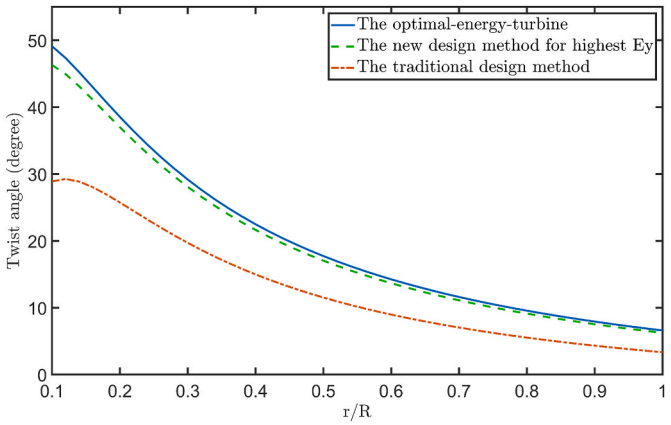

Fig. 21. The twist angle comparison.

Likewise, Fig. 22 and Fig. 23 compare the dimensionless chord length ($\frac{C}{R}$) and the twist angle (β) along the radius between the optimal-power-turbine found amongst all the possible designs, the turbine designed with the optimal a for power based on the expanded actuator disk theory and the turbine designed with $a = 1/3$.

5. Conclusions

This paper induces a new type of turbine, namely the force-driven turbine and explains the fundamental difference from the velocity-driven turbine. The paper expanded the actuator disk theory and further developed the BEMT design method for this kind of turbine. With a verification study conducted, the developed theories and methods have been verified. Based on this study, the following conclusions can be achieved.

1. The force-driven turbine is driven by a constant force, which is fundamentally different from the velocity-driven turbine which is driven by a constant velocity.
2. Based on the expanded actuator disk theory, the $a = \frac{1}{3}$ no longer leads to the highest P nor the highest E_y for the force-driven turbine. Betz's theory for velocity-turbine design do not apply to the force-driven turbine.
3. After the expansion of actuator disc theory, it is found that the power P is a function of B, ρ, R, r, C_d, a and the E_y is a function of B, L, R, r, C_d, a. High power turbine design doesn't lead to a high-energy turbine design. Therefore, two different optimal design targets have been proposed.

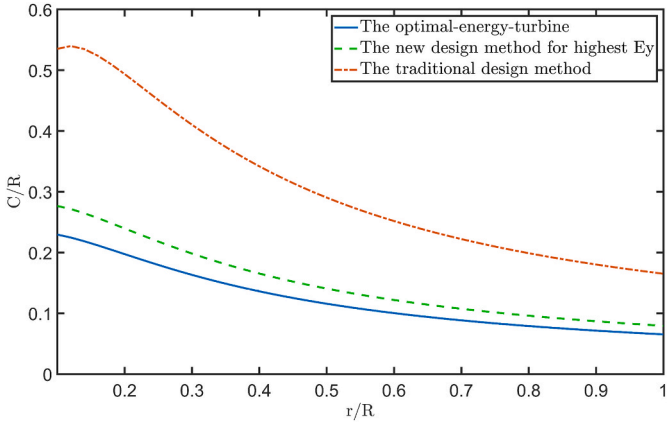

Fig. 20. The dimensionless chord length comparison.

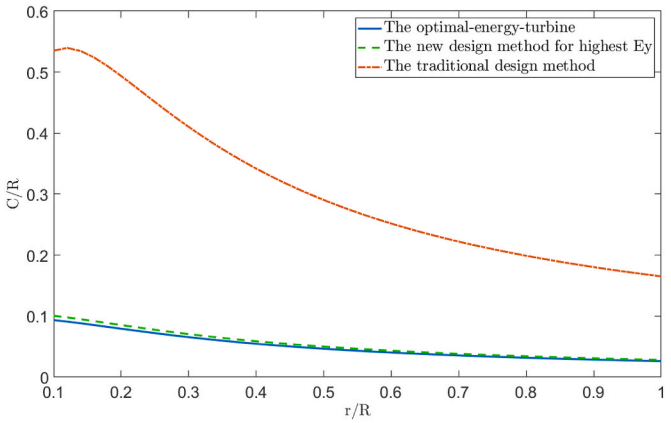

Fig. 22. The dimensionless chord length comparison.

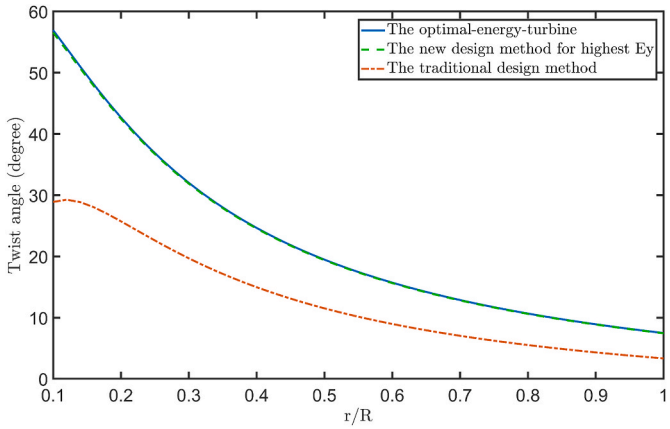

Fig. 23. The twist angle comparison.

4. New theoretical upper bounds of the energy conversion efficiency and the power of the energy harvest mechanism have been identified for the force-driven turbine to guide the design.
5. A new BEMT-based design method for the preliminary design of the force-driven turbine has been developed. The method can design the turbine according to the design aims, including designing the turbine with the highest E_y or designing the turbine with the highest P.
6. The verification study has been conducted with the BEMT method to design and simulate all the possible designs in all the possible operating conditions. The results have been compared with the expanded actuator disk theory and found the developed method is highly effective in identifying the optimal designs. Although there are some idealizations in the case study, such as ignoring the hydrodynamic effects of the wake, these idealizations do not affect the overall conclusions.

Based on this paper's study, the design method of the force-driven turbine has been developed, which is expected to contribute to the future design and development of force-driven turbines.

CRediT authorship contribution statement

Hongbo Hou: Writing – original draft, Methodology, Conceptualization, Validation, Formal analysis. **Weichao Shi:** Conceptualization, Writing – review & editing, Supervision, Project administration, Funding acquisition. **Yunxin Xu:** Formal analysis, Hydrodynamic analysis and simulation. **Yang Song:** Formal analysis, Underwater glider system design and analysis.

Declaration of competing interest

The authors declare that they have no known competing financial interests or personal relationships that could have appeared to influence the work reported in this paper.

Data availability

Data will be made available on request.

Appendix

The appendix shows the CFD simulation domain and boundary conditions of the UG hull.

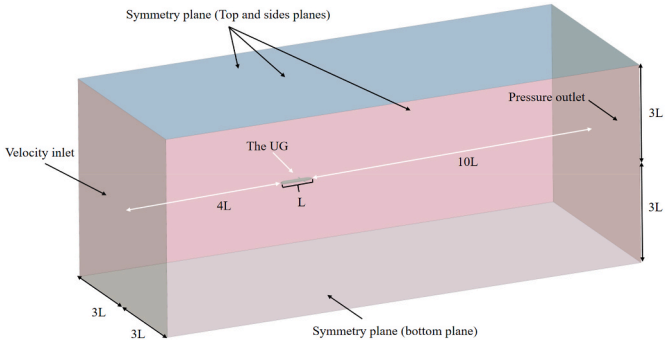

Fig. 24. Domain and boundary conditions of the CFD simulation.

References

Andersen, C., 2017. Why aren't primed mortars used as grenades? [Online]. Quora. Available: https://www.quora.com/Why-arent-primed-mortars-used-as-grenades/answer/Craig-Andersen-7, 2017].

Batchelor, G.K., 2000. An Introduction to Fluid Dynamics. Cambridge University Press, Cambridge.

Betz, A., 1920. Das maximum der theoretisch moglichen Auswendung des Windes durch Windmotoren, vol. 26. Zeitschrift fur gesamte Turbinewesen.

Boersma, S., Doekemeijer, B.M., Gebraad, P.M.O., Fleming, P.A., Annoni, J., Scholbrock, A.K., Frederik, J.A., Wingerden, J.W.V., 2017. A tutorial on control-oriented modeling and control of wind farms. In: 2017 American Control Conference (ACC), 24-26 May 2017, pp. 1–18.

Buhl, M.L., 2005. New Empirical Relationship between Thrust Coefficient and Induction Factor for the Turbulent Windmill State.

Burton, T., Jenkins, N., Sharpe, D., Bossanyi, E., 2011. Wind Energy Handbook. John Wiley & Sons.

Bzuk, 2003. Me 163 Komert at Canada Aviation Museum.

CCTV, 2019. Pufferfish unmanned helicopter [Online]. Available: https://space.bilibili.com/222103174 ([Accessed]).

Chao, Y., 2016. Autonomous Underwater Vehicles and Sensors Powered by Ocean Thermal Energy. OCEANS 2016 - Shanghai, 10-13 April 2016, pp. 1–4.

Corten, G.P., Schaak, P., 2008. Method and installation for extracting energy from a flowing fluid. Google Patents.

Das Karmakar, S., Chattopadhyay, H., 2022. A review of augmentation methods to enhance the performance of vertical axis wind turbine. Sustain. Energy Technol. Assessments 53, 102469.

De Lellis, M., Reginatto, R., Saraiva, R., Trofino, A., 2018. The Betz limit applied to airborne wind energy. Renew. Energy 127, 32–40.

Dixon, S.L., Hall, C.A., 2010. Chapter 10 - wind turbines. In: Dixon, S.L., Hall, C.A. (Eds.), Fluid Mechanics and Thermodynamics of Turbomachinery, sixth ed. Butterworth-Heinemann, Boston.

El Khchine, Y., Sriti, M., 2017. Tip loss factor effects on aerodynamic performances of horizontal Axis wind turbine. Energy Proc. 118, 136–140.

Encarnacion, J.I., Johnstone, C., Ordonez-Sanchez, S., 2019. Design of a horizontal Axis tidal turbine for less energetic current velocity profiles. J. Mar. Sci. Eng. 7.

English, W. H. Fighter Aircraft.

Froude, W., 1878. On the Elementary Relation between Pitch, Slip and Propulsive Efficiency, vol. 19. Transaction of the Institute of Naval Architects, pp. 22–33.
Glauert, H., 1935. Airplane Propellers. *Aerodynamic Theory*. Springer.
Gunston, B., 2000. The Osprey Encyclopedia of Russian Aircraft. Osprey Publishing.
Houck, D., Cowen, E.A., 2022. Power and flow analysis of axial induction control in an array of model-scale wind turbines. Energies 15, 5347.
ITTC, R., 2011. Procedures and Guidelines: Practical Guidelines for Ship CFD Applications, 7.5. ITTC, Boulder, CO, USA.
Jian, W., 2016. Research on several similarity criteria of ram air turbine operating under high-low altitude. In: 2016 IEEE International Conference on Aircraft Utility Systems (AUS), 10-12 Oct. 2016, pp. 141–145.
Jones, C., Allsup, B., Decollibus, C., 2014. Slocum Glider: Expanding Our Understanding of the Oceans. 2014 Oceans - St. John's, 14-19 Sept. 2014, pp. 1–10.
Jones, J.A., Chao, Y., 2006. Underwater Vehicle Propulsion and Power Generation. US7353768B1.
Ma, Z., Wang, Y., Wang, S., Yang, Y., 2016. Ocean thermal energy harvesting with phase change material for underwater glider. Appl. Energy 178, 557–566.
Rankine, W.J.M., 1865. On the Mechanical Principles of the Action of Propellers, vol. 6. Transaction of the Institute of Naval Architects, pp. 13–39.
Saad, M.M.M., Mohd, S., Zulkafli, M.F., Samiran, N.A., Didane, D.H., 2021. CFD simulation study on the performance of a modified ram air turbine (RAT) for power generation in aircrafts. Fluid 6, 391.
Saad, M.M.M., Mohd, S.B., Zulkafli, M.F., 2017. A survey on the use of ram air turbine in aircraft. In: AIP Conference Proceedings. AIP Publishing LLC, 020048.
SASHAX41, 2019. Ram Air Turbine (RAT) Emergency Power Supply in Case Power Loss.
Shen, W.Z., Mikkelsen, R., Sørensen, J., Bak, C., 2005. Tip loss correction for wind turbine computations. Wind Energy 8, 457–475.
Shi, W., Hou, H., Xu, Y., Mehmet, A., 2022. A New Thermal Buoyancy Engine and its Control Method. GB2010890, vol. 8.
Tony Burton, N.J., David, Sharpe, Ervin, Bossanyi, 2011. Aerodynamics of Horizontal Axis Wind Turbines. Wind Energy Handbook.
Van Der Hoek, D., Kanev, S., Allin, J., Bieniek, D., Mittelmeier, N., 2019. Effects of axial induction control on wind farm energy production - a field test. Renew. Energy 140, 994–1003.
Wang, G., Yang, Y., Wang, S., 2020. Ocean thermal energy application technologies for unmanned underwater vehicles: a comprehensive review. Appl. Energy 278, 115752.
Wang, G., Yang, Y., Wang, S., Zhang, H., Wang, Y., 2019. Efficiency analysis and experimental validation of the ocean thermal energy conversion with phase change material for underwater vehicle. Appl. Energy 248, 475–488.
Webb, D.C., Simonetti, P.J., Jones, C.P., 2001. SLOCUM: an underwater glider propelled by environmental energy. IEEE J. Ocean. Eng. 26, 447–452.
Yang, Y., Wang, Y., Ma, Z., Wang, S., 2016. A thermal engine for underwater glider driven by ocean thermal energy. Appl. Therm. Eng. 99, 455–464.
Zhao, D., Han, N., Goh, E., Cater, J., Reinecke, A., 2019. Chapter 1 - general introduction to wind turbines. In: Zhao, D., Han, N., Goh, E., Cater, J., Reinecke, A. (Eds.), Wind Turbines and Aerodynamics Energy Harvesters. Academic Press.